

# Numerical Study of the Current-Voltage Characteristic of Hall Thrusters

S. Barral, K. Makowski, Z. Peradzyński\*

Institute of Fundamental Technological Research - PAS

Świętokrzyska 21, 00-049 Warsaw, Poland

\*also: Dept. of Mathematics, Informatic and Mechanics of Warsaw University

Banacha 2, 00-097 Warsaw, Poland

e-mail: sbarral@ippt.gov.pl, kmak@ippt.gov.pl, zperadz@ippt.gov.pl

N. Gascon<sup>†</sup>, M. Dudeck

CNRS Laboratoire d'Aérothermique

1c avenue de la Recherche Scientifique, 45071 Orléans, France

<sup>†</sup>current address: Stanford University, Mechanical Engineering Department

Stanford - California 94305-3032, USA

e-mail: nicolas@navier.stanford.edu, dudeck@cnrs-orleans.fr

IEPC-01-27

**The Current-Voltage characteristic of a Hall Thruster of type SPT-100ML was analyzed with a 1D numerical model, and confronted to experimental results obtained with channels made of different materials. A strong correlation was found between the appearance in simulations of a space-charge limited sheath at the walls and a low frequency mode observed in experiments characterized by a high discharge current. Simulations show that depending on the electron emission characteristics of the material of the channel, a discharge voltage threshold exists beyond which the space charge limited sheath at the walls occurs and induces an electronic avalanche responsible for a high total current and high Joule losses. It is suggested that the secondary electron emission yield is not the single parameter characterizing materials, and that backscattering of electrons by the walls could play an equally fundamental role.**

## 1 Introduction

Experimental measurements led in the Pivoine facility (CNRS-France) on a SPT-100ML thruster have clearly emphasized the fundamental role played by the material of the discharge channel on the global characteristics and performances of the engine [1]. These experiments have as well shown that the average value of the discharge current and its frequency spectrum strongly differ from one material to another.

The near-wall conductivity has always been suspected to provide a large contribution to the global electric conductivity, at least at high voltages. Secondary electron emission has been pointed as one of the main

parameters determining the details of the near-wall processes. It has been as well suggested recently [3] that the potential of the sheath at the walls may become saturated when the temperature of the plasma is such that the secondary electron emission yield approaches 1, thus preventing the sheath from collapsing.

In a previous work [2] the effect of secondary emission on the performances of Hall thrusters was analyzed using a transient 1D fluid model with a simple description of the sheath at the walls. Although the global efficiency predictions were consistent with measured data, the differences of operating modes observed in experiments when using channels made of alumina or boron nitride could not be satisfactorily explained.

For the present study, the former fluid model has been improved on several key points, including in particular a more detailed description of the sheath and the

---

Copyright © 2000 by Institute of Fundamental Technological Research - Polish Academy of Science. Published by the Electric Rocket Propulsion Society with permission.

presheath. Other improvements concern the addition of an energy equation for ions and a two-populations transport model for neutrals taking into account scattering at the walls. Besides, an accurate and stable Flux-Splitting type scheme has been implemented for the transport of ions, based on the solver of Roe.

## 2 Transient 1-D fluid model

### 2.1 Governing equations for neutrals

A significant increase of the mean axial velocity of neutrals can be expected within the channel since on one hand ionization acts as a selection process by removing primarily slow neutrals and letting mainly fast neutrals to reach the exit, and on the other hand scattering of neutrals by the walls gives rise to a reverse flow which reduces the mean velocity upstream. A simple, yet realistic two-population model accounting for these phenomena has been developed and tested by comparison with exact solutions and with a 2D-axisymmetric Ray-tracing/Monte-Carlo model.

A detailed justification of this model is beyond the scope of this paper, but the rationale behind the division into two populations is the following: the first population shall represent neutrals emitted by the gas feed and retain those which are reflected in a specular way by the walls, while neutrals randomly scattered by the walls shall be transferred into a second population considered to be in thermal equilibrium with the walls.

Assuming that the initial density distribution near the gas feed is Maxwellian and isotropic (retaining only particles with positive axial velocities), it can be shown that in the steady state the dispersion of velocities in the axial direction remain almost constant in spite of ionization at  $\frac{kT_c}{3m_a}$ , where  $T_c$  is the temperature of the channel (considered equal to the temperature of the gas feed) and  $m_a$  the mass of neutrals. This leads to the following set of equations for the first population:

$$\frac{\partial n_{a1}}{\partial t} + \frac{\partial(n_{a1}V_{a1})}{\partial x} = -\beta n_e n_{a1} - \alpha_{scat} \gamma_{wall}(x) \cdot n_{a1} V_{a1} \quad (1)$$

$$\frac{\partial(n_{a1}V_{a1})}{\partial t} + \frac{\partial(n_{a1}V_{a1}^2 + n_{a1}\frac{kT_c}{3m_a})}{\partial x} = -\beta n_e n_{a1} V_{a1} - \alpha_{scat} \gamma_{wall}(x) \cdot n_{a1} V_{a1}^2 \quad (2)$$

where  $n_{a1}$  and  $V_{a1}$  refer to the density and mean axial velocity of neutrals respectively, and  $n_e$  to the density of electrons. The accommodation parameter  $\alpha_{scat}$  lies between 0 for a perfectly rough wall to 1 for a perfectly smooth wall.  $\beta$  is the ionization rate, taken as a function of electron temperature and drift energy; it is computed assuming a drifted Maxwellian distribution using the cross-sections from [4].

The transfer of particles to the second population is determined by a view factor which in the case of an axisymmetric channel is well approximated by:

$$\gamma_{wall}(x) = \frac{x}{\left(\frac{R_2 - R_1}{2}\right)^2 + x^2} \quad (3)$$

where  $R_1$  and  $R_2$  are respectively the inner and outer radii of the channel.

The boundary conditions for the first population are:

$$\begin{cases} V_{a1}|_{x=0} = \sqrt{\frac{2kT_c}{\pi m_a}} \\ n_{a1}V_{a1}|_{x=0} = \frac{Q}{m_a \cdot S} \end{cases} \quad (4)$$

where  $Q$  is the net mass flow rate of particles injected inside the channel, and  $S$  the cross-section of the channel.

The second population is assumed to be in thermal equilibrium with the walls, which yields the following transport equations:

$$\frac{\partial n_{a2}}{\partial t} + \frac{\partial(n_{a2}V_{a2})}{\partial x} = -\beta n_e n_{a2} + \Gamma_{iw} + \alpha_{scat} \gamma_{wall}(x) \cdot n_{a1} V_{a1} \quad (5)$$

$$\frac{\partial(n_{a2}V_{a2})}{\partial t} + \frac{\partial(n_{a2}V_{a2}^2 + n_{a2}\frac{kT_c}{m_a})}{\partial x} = -\beta n_e n_{a2} V_{a2} - \alpha_{scat} \nu_{wall} n_{a2} V_{a2} \quad (6)$$

where  $\Gamma_{iw}$  is the flux of ions neutralized on the walls and  $\nu_{wall}$  is the collision frequency of neutral particles with the wall, given by:

$$\nu_{wall} = \frac{\sqrt{\frac{2kT_c}{\pi m_a}}}{R_2 - R_1} \quad (7)$$

Note that particles of the second population, either scattered or specularly reflected on the walls, remain in this same population.

The boundary conditions are a sonic point at  $x = L$  (due to the expansion toward vacuum), and a zero net flux at  $x = 0$ .

$$\begin{cases} \mathcal{M}_2|_{x=L} = \frac{V_{a2}|_{x=L}}{\sqrt{\frac{kT_c}{m_a}}} = 1 \\ n_{a2}V_{a2}|_{x=0} = 0 \end{cases} \quad (8)$$

Comparisons with exact solutions and Monte-Carlo simulations in the steady-state case for different values of ionization frequency have shown a near-perfect fit between the model and reference solutions. This model was also compared with exact solutions derived assuming a sinusoidal time-varying ionization in the presence of perfectly smooth walls, and proved to be robust with regard to transient effects.

## 2.2 Governing equations for ions

The transport of ions is described by the first three moments of Boltzmann equation assuming a free fall:

- mass conservation:

$$\frac{\partial n_i}{\partial t} + \frac{\partial (n_i V_i)}{\partial x} = \beta n_a n_e - \Gamma_{iw} \quad (9)$$

- momentum conservation along the main axis:

$$\frac{\partial (n_i V_i)}{\partial t} + \frac{\partial \left( n_i V_i^2 + 2n_i \frac{D_i}{m_i} \right)}{\partial x} = \frac{n_i e E}{m_i} + \beta n_a n_e V_a - \Gamma_{iw} V_i \quad (10)$$

- energy conservation:

$$\frac{\partial \left( \frac{1}{2} n_i V_i^2 + n_i D_i \right)}{\partial t} + \frac{\partial \left( \frac{1}{2} n_i V_i^3 + 3n_i V_i \frac{D_i}{m_i} \right)}{\partial x} = n_i V_i \frac{eE}{m_i} + \beta n_a n_e \frac{V_a^2}{2} - \Gamma_{iw} \left( \frac{V_i^2}{2} + \frac{D_i}{m_i} \right) \quad (11)$$

where  $m_i$  is the mass of ions,  $E$  the axial electric field,  $\Gamma_{iw}$  the flux of ions to the walls per unit length,  $n_i$  the density of ions,  $V_i$  the mean velocity of ions in

the axial direction, and  $D_i$  the non-directed energy resulting from the dispersion of axial ion velocities, i.e.  $D_i = \frac{1}{n_i} \int_{-\infty}^{+\infty} f_i \cdot \frac{1}{2} m_i (v_i - V_i)^2 \cdot dv_i$ , while  $n_a$  stands for the total density of neutrals and  $V_a$  for their mean velocity.

Note that the quantity  $\int_{-\infty}^{+\infty} f_i \cdot \frac{1}{2} (v_i - V_i)^3 \cdot dv_i$  was neglected in the space derivative of the energy equation. In a free fall model, this assumption is only valid if it can be assumed that the velocity distribution is symmetric or if  $D_i$  is small with respect to the directed energy. This assumption does not hold in the ionization zone, but the dispersion of velocities is very small in this region so that the electron pressure gradient which appears after substitution of the electric field by Ohm law in Eq. (10) largely outweighs the gradient of  $n_i D_i$  and the inaccuracies on  $D_i$  are therefore practically harmless. On the other hand, it is known from experiments [5, 6] that the ion velocity distribution is close to symmetric and is quite narrow in the acceleration zone, where the influence of the gradient of  $n_i D_i$  on the momentum equation is greater. The value of  $D_i$  at the exit of the channel generally lies within 5 – 10% of the directed kinetic energy.

## 2.3 Governing equations for electrons

The following stationary equations are used to describe the transport of electrons:

- momentum conservation along the main axis (Ohm law):

$$\frac{d \left( n_e \frac{kT_e}{m_e} \right)}{dx} = - \frac{n_e e E}{m_e} + n_e \omega_B V_{e\theta} - (k_m n_a n_e + \Gamma_{ew}) V_{ez} \quad (12)$$

- momentum conservation along the azimuth:

$$\frac{d (n_e V_{ez} V_{e\theta})}{dx} = - n_e \omega_B V_{ez} - (k_m n_a n_e + \Gamma_{ew}) V_{e\theta} \quad (13)$$

- entropy-like energy equation (see [7]):

$$\frac{d \left( \frac{(kT_e)^{\frac{3}{2}}}{n_e} \right)}{dx} = - \frac{\sqrt{kT_e}}{V_e n_e} [ Q_{Joules} - Q_{ioniz} - Q_{wall} - Q_{heating} ] \quad (14)$$

with:

$$Q_{Joules} = (k_m n_a n_e + \Gamma_{ew}) E_{ke}$$

$$Q_{ioniz} = \gamma_{ion} e U_{ion} \beta n_a n_e$$

$$Q_{wall} = \Gamma_{ew} [E_{ke} + 2kT_e + e\phi_w] - \Gamma_{ew} [\varepsilon_{bs}(E_{ke} + 2kT_e) + \overline{\delta_{eff}} |\phi_w|]$$

$$Q_{heating} = (\beta n_a - \Gamma_{iw}) \left( \frac{5}{2} kT_e - E_{ke} \right)$$

where  $V_{e\theta}$  and  $V_{ez}$  are the electron velocity components in the azimuthal and axial direction,  $T_e$  is the temperature of electrons,  $E_{ke}$  is the drift energy of electrons,  $\Gamma_{ew}$  is the flux per unit length of electrons colliding with the walls,  $k_m$  is the total momentum transfer rate by electron/neutral collisions given as a function of  $T_e$  and  $E_{ke}$  (computed on the basis of the ionization cross-sections and elastic collision momentum transfer cross-section from [8]),  $\omega_B$  is the Larmor frequency,  $U_{ion}$  is the ionization potential of xenon,  $\gamma_{ion}$  is the factor of effective ionization cost, and  $\phi_w$  is the potential drop across the sheath.

For a shifted Maxwellian distribution, the average energy of electrons colliding with the walls is equal to  $2kT_e + E_{ke}$  (provided that the direction of the drift is parallel to the walls), hence the factor  $E_{ke} + 2kT_e + e\phi_w$  in the term  $Q_{wall}$  since losses are evaluated at the sheath edge.

The parameter  $\overline{\delta_{eff}}$  is the macroscopic effective secondary electron emission yield, i.e. the secondary electron emission yield averaged over the distribution function of electrons. This yield accounts for both true secondary electrons and backscattered electrons (elastically and inelastically scattered).

The parameter  $\tau_{bs}$  is the backscattered energy yield which represents the ratio between the flux of energy towards the walls and the flux of energy re-emitted from the walls. This factor is considered constant, which is probably only a very rough approximation of the reality since the elastic and inelastic electron backscattering yields are known to behave in a complex manner in the low energy range, notwithstanding the non-trivial dependence of the incidence angle at low energies [9]. There seems to be close to none literature about backscattering yields and backscattered electrons

energy spectrum for energies of primary electrons below  $100eV$ , and  $\tau_{bs}$  must therefore be determined empirically following a few ‘‘rules of thumb’’. A higher limit of the parameter  $\tau_{bs}$  is obtained by considering the (improbable) case were only elastic backscattering takes place, which implies that the following condition should be met:

$$\tau_{bs} < \min \overline{\delta_{eff}}$$

Furthermore, it is assumed that the backscattered energy yield is a decreasing function of the mean atomic number. This was verified at least for primary electrons with energy of the order of the  $keV$ , for which it was observed that the yield of backscattered electrons increases with the mean atomic number of the material of the wall [10], while the energy spectrum of backscattered electrons is shifted to higher energies for heavier elements [11].

## 2.4 Wall sheath and presheath description

### 2.4.1 Model of presheath

The derivation of the whole model of presheath is expected to be published in a separate paper [12], and will therefore not be detailed here. The starting point to solve the presheath are the continuity equation and radial momentum conservation for ions completed by the conservation of azimuthal momentum for electrons. In cylindrical coordinates and after a few simplifications, these equations read:

$$\frac{\partial n_i}{\partial t} + \frac{\partial (n_i V_{ir})}{\partial r} + \frac{\partial (n_i V_{ix})}{\partial x} + \frac{n_i V_{ir}}{r} = \beta n_a n_i \quad (15)$$

$$\frac{\partial n_i V_{ir}}{\partial t} + \frac{\partial (n_i V_{ir}^2)}{\partial r} + \frac{\partial (n_i V_{ir} V_{ix})}{\partial x} = \frac{e E_r n_i}{m_i} \quad (16)$$

$$kT_e \frac{\partial n_e}{\partial r} = -n_e e E_r \quad (17)$$

The centrifugal force due to  $V_{e\theta}$  was neglected in the last equation, since computations including it were performed which showed that its effect is generally weak.

It was assumed that the quantities  $n_i$ ,  $V_{ir}$  and  $E_r$  can be expressed as follows:

$$n_i(x, r, t) = f(r) \cdot n_i(x, t)$$

$$V_{ir}(x, r, t) = g(r) \cdot V_B(x, t)$$

$$E_r(x, r, t) = E_r(r)$$

where  $V_B$  denotes the Bohm velocity (defined later in the model of the sheath).

Additionally, the quantities  $V_{ix}$ ,  $T_e$ ,  $\beta$  and  $n_a$  are considered independent of  $r$ .

The boundary conditions are derived assuming that ions reach exactly Bohm velocity at the sheath edges, hence:

$$\begin{aligned} V_{ir}|_{r=R_1} &= -V_B \\ V_{ir}|_{r=R_2} &= V_B \end{aligned}$$

Assuming quasi-neutrality in the presheath, the problem stated above can be solved numerically and lets us derive a factor  $\chi$  such that the integral of Eq. (15) over the cross-section is expressed as:

$$\frac{\partial \langle n_i \rangle}{\partial t} + \frac{\partial (\langle n_i \rangle V_{ix})}{\partial x} = \beta n_a \langle n_i \rangle - \chi \langle n_i \rangle \frac{2V_B}{R_2 - R_1} \quad (18)$$

This is actually the same equation as Eq. (9) with an emphasis on the fact that  $\langle n_i \rangle$  (called simply  $n_i$  in previous sections) is the ion density averaged over the cross-section.

Interpreting the factor  $\frac{2V_B}{R_2 - R_1}$  as the collision frequency of ions with the walls in a cylindrical geometry, the parameter  $\chi$  can then be understood as the rate between the density at the sheath edge and the average density in the corresponding cross-section. Its actual meaning is in fact slightly more complicated, since ion densities at the inner and outer sheath edges differ in cylindrical geometry.

In general,  $\chi$  is a function of two parameters, but in the planar approximation ( $\frac{R_1}{R_2 - R_1} \rightarrow \infty$ ) it can be found as a function of a single parameter  $C$ , and is given implicitly by the relationship:

$$\arctan \sqrt{\frac{C}{\chi}} - \frac{C+1}{C+\chi} \sqrt{C\chi} = 0 \quad (19)$$

where:

$$C = \frac{(R_2 - R_1)}{2V_B} \left[ \beta n_a + \frac{1}{V_B} \frac{\partial V_B}{\partial t} + \frac{V_{ix}}{V_B} \frac{\partial V_B}{\partial x} \right]$$

A fairly good approximation of the solution of Eq. (19) is given by:

$$\tilde{\chi}(C) = \frac{1}{\frac{3}{2} + \frac{4C}{\pi^2}} \quad (20)$$

which verifies:

$$\begin{aligned} \lim_{C \rightarrow 0} \tilde{\chi} &= \lim_{C \rightarrow 0} \chi \\ \lim_{C \rightarrow \infty} \frac{\tilde{\chi}}{\chi} &= 1 \\ \sup_{C \in (0, +\infty)} \left| \frac{\tilde{\chi} - \chi}{\chi} \right| &< 0.023 \end{aligned}$$

The maximal relative error made when approximating the axisymmetric solution (without centrifugal force) with the exact planar solution is lower than 3.5% if  $\frac{R_1}{R_2 - R_1} > \frac{1}{2}$ . In the case of the SPT-100ML the ratio  $\frac{R_1}{R_2 - R_1}$  is about  $\frac{3}{2}$  and the planar approximation is thus well justified. For the sake of simplicity, the convection terms in the expression of  $C$  were neglected in the global model of the discharge.

A model of presheath was recently independently derived by other authors [13] in planar geometry. Although the approach taken seems to be slightly different, it results in an equation equivalent to Eq. (19).

#### 2.4.2 Model of sheath

The phenomenological behavior of the sheath potential  $\phi_w$  in the presence of secondary electron emission (SEE) has been described recently in [3]. It was found that as one may expect, the ratio  $\frac{|\phi_w|}{T_e}$  decreases when the SEE yield increases, but as the SEE yield reaches a value close to 1 the potential of the wall suddenly saturates due to the appearance of a so-called ‘‘virtual cathode’’, which actually corresponds to a local minimum of the potential behind which electrons are trapped in the close vicinity of the walls that the ratio between incoming and outgoing electron fluxes remain constant.

The model of sheath used in this study is based on the fluid approach described by Hobbs and Wesson [14], and will therefore not be justified with great details here. The model of Hobbs and Wesson did not treat the effect of backscattering and assumed therefore that electrons have a negligible velocity when leaving the walls. It can be verified, however, that the effect of backscattering on the sheath can be well approximated by simply defining an effective SEE yield which includes the backscattering yield.

In theory, when secondary emission is taken into account the Bohm condition slightly differs from its classical form [14]. The classical Bohm condition constitutes

nevertheless a reasonable approximation of the modified one, and Bohm velocity was therefore taken as usual as:

$$V_B \approx \sqrt{\frac{kT_e}{m_i}} \quad (21)$$

Similarly, it can be shown that the expression of the sheath potential is reasonably approximated by the classical expression derived e.g. in [2] which reads:

$$\phi \approx -\frac{kT_e}{e} \ln \left[ (1 - \delta_{eff}) \sqrt{\frac{m_e}{2\pi m_i}} \right] \quad (22)$$

The space-charge limited regime occurs when the electric field becomes zero at the wall. Solving numerically the integral form of Poisson equation given in [14], one may derive an approximate expressions of the value of the sheath potential in the space-charge limited regime:

$$(\phi_w)_{sat} \approx -\frac{kT_e}{e} \left( 3.37 \sqrt{\frac{m_e}{m_i}} - 1.025 \right) \quad (23)$$

which in the case of Xenon gives  $(\phi_w)_{sat} \approx -1.02 \frac{kT_e}{e}$ , corresponding to a critical value of effective SEE yield  $(\overline{\delta_{eff}})_{sat} \approx 0.98$ . These values are consistent with those found with a kinetic approach [3].

In the space charge limited regime, the values of potential and effective SEE yield remain equal to the critical values whatever the real value of the secondary electron emission. The potential well located beyond the virtual cathode ensures that the effective SEE yield seen at the level of the virtual cathode remain constant.

It can be noted at this point that the potential well formed between the local minimum of potential and the wall does not need to be studied in details, since its magnitude (in term of potential) is of the order of the energy of secondary electrons, i.e. a fraction of  $V$ . It could be objected that since backscattered electrons are re-emitted with an energy of the order of the plasma temperature, the potential of the well might actually be higher, but since the backscattering yield is in practice always lower than  $(\overline{\delta_{eff}})_{sat}$  by a factor at least 2, the potential well needs only to capture secondary electrons to ensure the condition  $\overline{\delta_{eff}} = (\overline{\delta_{eff}})_{sat}$  and the potential drop across the well is thus always very small.

In any regime (classical or space charge limited), the flux of electrons per unit length incident on the walls is given by:

$$\Gamma_{ew} = \chi \langle n_i \rangle \frac{2}{R_2 - R_1} \sqrt{\frac{kT_e}{2\pi m_e}} e^{\frac{e\phi_w}{kT_e}} \quad (24)$$

By identifying Eq. (9) and Eq. (18), one obtains the flux of ions to the walls per unit length:

$$\Gamma_{iw} = \chi \langle n_i \rangle \frac{2}{R_2 - R_1} V_B$$

### 2.4.3 Effective SEE yields

The effective microscopic secondary electron emission yield  $\delta_{eff}$  is estimated from experimental data given in the range 20 – 100eV, which do not distinguish between true secondary emission backscattering. There exist many theories concerning the secondary electron emission yield, but the lack of reliable data about SEE yields in the low energy range and the fact that these theories only account for true secondary electrons while backscattering is probably dominant at low energies make it very difficult to privilege one approach. The best fit of experimental data used for this study is from far a straight line and nothing suggests a fast decay of the SEE yield in the neighborhood of the origin. This was also mentioned in [15] where it was suggested to take  $\delta_{eff}(0) \approx 0.5$  for ceramics, which seems consistent with our values. The values of  $\delta_{eff}(0)$  that we found by linear regression were correlated with the mean atomic number  $\bar{Z}$  of the material (high  $\bar{Z}$  materials presenting higher  $\delta_{eff}(0)$ ) which seems to justify the hypothesis of dominating backscattering, but this correlation might be coincidental since only three materials were studied.

The SEE yields were consequently defined like in [15] as:

$$\delta_{eff}(\varepsilon) = \delta_{eff}(0) + \frac{\varepsilon}{\varepsilon^*} [1 - \delta_{eff}(0)] \quad (25)$$

where  $\varepsilon$  is the energy of a primary electron and  $\varepsilon^*$  is the cross-over energy (i.e. such that  $\delta_{eff}(\varepsilon^*) = 1$ ).

Assuming a Maxwellian electron distribution function and a linear variation law for the SEE yield, the macroscopic effective SEE yield is related to the microscopic yield by the simple relationship  $\overline{\delta_{eff}} = \delta_{eff}(\bar{\varepsilon})$  where  $\bar{\varepsilon}$  is the average energy of electrons hitting the

walls. As stated earlier,  $\bar{\varepsilon}$  is independent of the sheath potential and is given by  $\bar{\varepsilon} = 2kT_e + E_{ke}$ . Note that in [3] the authors have proposed to take  $\bar{\varepsilon}$  as  $2kT_e + 2E_{ke}$  in the presence of a  $E \times B$  drift based on the discussion given in [18], but this may arise from a different interpretation of the meaning of the temperature. In our understanding the parameter  $T_p$  as defined in [18] characterizes only the velocity dispersion of newly born electrons or of electrons having just collided, whereas notwithstanding the real shape of the electron distribution function, one usually defines the temperature of electrons  $T_e$  such that it accounts for the totality of the non-directed energy and as such the quantity  $\frac{3}{2}kT_e$  already includes a part of energy approximately equal to  $E_{ke}$  due to the non-directed energy contribution of the Larmor motion.

## 2.5 Parameters and boundary conditions

The propellant considered for all computations and experimental results reported in this study is xenon.

Boundary conditions for the flow of neutrals are determined from the average temperature of the channel  $T_c$ , taken equal to  $800K$ .

The reference profile of magnetic field is approximated by a Gaussian profile of the form:

$$B_r(x) = B_{min} + (B_{max} - B_{min}) \frac{e^{-\frac{1}{W_B^2} (1 - \frac{x}{L})^2} - e^{-\frac{1}{W_B^2}}}{1 - e^{-\frac{1}{W_B^2}}}$$

where  $W_B$  is the dimensionless width of the magnetic region.

In the following discussion,  $W_B^0$  refers to the nominal value of this parameter computed on the basis of experimental measurements of the magnetic field in the center of the channel. Upon mention, a slightly wider magnetic region is used by taking  $W_B = 1.2 \cdot W_B^0$ .

For ions, the sonic point condition similar to what was proposed in [19] was imposed at  $x = 0$ , i.e.:

$$V_i|_{x=0} = -\sqrt{\frac{5}{3} \frac{kT_e}{m_i} + 6 \frac{D_i}{m_i}} \quad (26)$$

It is not clear how realistic this condition is, since the axial drift of electrons which is neglected in this approach may be actually quite large due to the total absorption

of electrons at the boundary, and may lead to a significant modification of the boundary condition.

Before specifying other boundary conditions, it must be mentioned that this model is deliberately restricted to the study of the plasma within the channel, and does not intend to describe the acceleration experienced by ions beyond the exit of the channel. The justification of this choice is twofold:

1. A realistic description of the processes taking place in this region is probably out of reach for a 1D model. The behavior of the plume is strongly dependent on the topology of the magnetic field, and the expansion of the plasma is therefore a purely two-dimensional transport problem involving complex electron-wall interactions on the surfaces covering magnetic poles. Spectroscopic measurement on an ATON class thruster [24] have shown that the discharge in the exit plane of the channel is far from uniform across the section. Relating these measurements with the magnetic field profile, it appears clearly that “short-circuits” exist (close to the inner wall in the case of an ATON) through which most electrons enter the channel without experiencing a significant potential drop. By contrast, ions very likely flow through the whole cross-section and are therefore on the average subjected to a large potential drop. These disparate behaviors seem difficult to synthesize in a 1D model.
2. The 1D description of the plasma inside the channel is only weakly influenced by the region beyond exit, except for the subsequent decrease of potential drop. Indeed, ions are supersonic and neutrals are either sonic (second population) or supersonic (first population) when leaving the channel, so that no information can propagate upwind. Moreover the large magnetic field in the exit plane implies that the drift energy and temperature of electrons are determined nearly locally [7]. Since simulations show that the profile of potential remains almost stationary even in strong oscillatory regime and that ionization is almost inexistent in the plume, it seems reasonable to assume that the potential drop in the plume is constant and to simply shift and/or re-scale *a posteriori* the simulated

current-voltage characteristic, possibly on the basis of experimental measurements of the potential drop in the plume. Note, however, that such correction will not be attempted in the present work.

In the light of the discussion above, the potential drop is prescribed between anode and exit plane, and implicitly determines the total discharge current  $I_d$  via the following relation, obtained from Eq.(12):

$$U_d = - \int_0^l \frac{1}{n_i} \frac{d(n_i k T_e)}{dx} dx + \int_0^l \frac{m_e}{m_i} \left( \nu_{tot} + \frac{\omega_B^2}{\nu_{tot}} \right) \left( \frac{I_d}{n_i e S} - V_i \right) dx \quad (27)$$

with  $\nu_{tot} = k_m n_a + \frac{\Gamma_{ew}}{n_e}$ .

Concerning electron transport, we have shown in a previous work [7] that there is no real need for a boundary condition on the electron temperature in the exit plane of the channel since the right hand side of Eq. (14) is the difference of two source terms each much larger than the left hand side if the magnetic field is strong enough (as it is the case in the exit plane), which implies that the temperature adjusts itself on a distance of the order of the millimeter. The boundary condition on the  $T_e$  can therefore be reliably estimated exclusively from the local parameters of the plasma by forcing the left hand side to zero. The same reasoning applies to Eq. (13) which determines the azimuthal drift velocity of electrons and the corresponding drift energy  $E_{ke}$ . Note that most authors have chosen to solve Eq. (13) locally throughout the channel and not only at the boundary as it is done here, but this approximation seems to fail in the reversed ion flow region close to anode.

Except when specifically mentioned, backscattering is neglected, i.e.  $\tau_{bs} = 0$ .

## 2.6 Computational methods

The flow of the first population of neutrals (fully supersonic) is solved using an Upwind scheme, and the flow of the second population (fully subsonic) with a McCormack scheme.

Prior to solving the transport of ions, the electric field was eliminated in Eq. (10) using Ohm law (12) and in Eq. (11) by combination with Eqs. (9) and (10). Using

the similarities between the resulting system of equations and Euler equations, a scheme derived from the scheme of Roe [21] was devised where the splitting of fluxes is based on the signs of the following eigenvalues:

$$\left\{ \begin{array}{l} \lambda_0 = V_i - \sqrt{\frac{5}{3} \frac{k T_e}{m_i} + 6 \frac{D_i}{m_i}} \\ \lambda_1 = V_i \\ \lambda_2 = V_i + \sqrt{\frac{5}{3} \frac{k T_e}{m_i} + 6 \frac{D_i}{m_i}} \end{array} \right\} \quad (28)$$

This scheme is not conservative as is the original Roe scheme, but it does fulfill the consistency requirement in a finite-difference formulation. Since we are only interested in continuous solutions and because the source terms are large, the lack of conservativity is not a concern here. The instability of the Roe scheme at the sonic point was corrected using the method of Harten [22].

## 3 Results

### 3.1 Scope

A number of works have been devoted to the numerical simulation of Hall thrusters, but presumably due to the computation times usually required, there have been only few attempts at studying the current-voltage characteristic (CVC) given by numerical models. One of the most successful attempt to date is perhaps that of J.P. Boeuf and L. Garrigues [23], who identified a region of spontaneous low frequency oscillations in the CVC which is very likely related to the low frequency oscillatory regime observed in experiments.

Many peculiarities of the CVC remain, however, without satisfactory explanation. Without being exhaustive, one can mention at least :

1. the local maximum of discharge current seen in the CVC of all SPT-class thrusters in the low-voltage region
2. the exact role of the material of the channel on the discharge and its impact on the CVC
3. the behavior of the fundamental frequency of the current oscillations as a function of the voltage and

in particular the origin of the decay of this frequency at high voltages

The first question has been discussed from a theoretical viewpoint by many authors, and several interpretations have been proposed for the so-called anomalous conductivity likely to explain the local maximum in the CVC. Most of these theories involve non-trivial oscillation mechanisms [25] and are therefore difficult to account for in a fast and reasonably simple model. A simpler explanation of the local maximum of discharge current has been proposed in [26] and involves mainly the non-monotonic dependence of the momentum transfer collision rate on the temperature. Although this explanation was supported by a mathematical model, its validity remains still unclear in regard to the reliance of these results on an adequate choice of boundary conditions and to the impossibility to reproduce such results in more complex models despite the use of similar operating conditions. This problem is thus considered out of the scope of the present study, and the following results indeed clearly underestimated the current at low voltage.

The second question and to a lesser extend the third question shall constitute the main object of the present study. The availability of experimental results [1] obtained within a wide range of discharge voltages with channels constituted from different materials give new perspectives for the theoretical and numerical study of the CVC, and make it in particular possible to assess the validity of the theory of sheath.

### 3.2 Method of frequency analysis

Due to the transient nature of the model, it appears interesting to study in parallel with the CVC the fundamental frequency of the discharge current. The computations do not necessarily lead to self-excited modes, and many of the results actually exhibit damped modes. The response of the model to a small disturbance is in the later case very informative, since as the signal gets small enough, the system becomes quasi-linear and the response (in term of discharge current) is that of a damped harmonic oscillator, that is:

$$I_d(t) = I_d^\infty + \Delta I_d e^{-d_0 \cdot t} \cos\left(\sqrt{(2\pi f_0)^2 + d_0^2} \cdot t + \Phi\right)$$

where  $d_0$  is the damping and  $f_0$  the eigenfrequency of the system.

Since the actual response is very close to the ideal response, the frequency analysis is performed using a function matching procedure. This method is much more accurate and reliable than a Fourier analysis for a damped signal.

The frequency reported in the results is the eigenfrequency  $f_0$ , but the damping is in general low enough to neglect the difference between the eigenfrequency and the frequency of the response.

It must be noted that in the neighborhood of the region of the CVC later referred to as the space charge limited sheath region, the transient response exhibits non-linear effects. Nevertheless, notwithstanding the non-sinusoidal shape of the response signal, the approximation with a damped harmonic oscillator remains relevant to predict the position of the extrema of the signal so that the frequency can still be unambiguously determined.

### 3.3 Qualitative comparison with anterior results

Due to the similarities between the SPT-100ML thruster and its close parent the SPT-100, a qualitative comparison with the results obtained by Boeuf and Garrigues for a SPT-100 with a hybrid model [23] is well justified.

The SPT-100 differs from the SPT-100ML mainly by the length of the active part of its channel and by a slightly stronger magnetic field. The geometrical differences have probably a limited effect on the results, but the higher magnetic field surely enhances plasma oscillations. In order to illustrate the parallel between both models, the width of the magnetic region was slightly increased by comparison with the nominal case, which has virtually the same effect as an increase of  $B_{max}$ . Self-excited oscillations would otherwise not appear in this range of voltage, which seems consistent with the observation made by Boeuf and Garrigues when lowering the value of  $B_{max}$ . The simulations were made using a material characterized by a low secondary electron emission (called *Mat-A* in the following sections).

There exists also very many differences at the level of the mathematical and numerical models. The model of Boeuf and Garrigues did not take into account ion losses at the walls where the sheath potential was considered constant, and the dependency of collision rates on the drift energy of electrons was neglected as well as

the electron pressure gradient in Ohm law. On the other hand, losses by excitations were described more accurately than in the present model. The transport of ions was based on a resolution of Vlassov equation with a finite difference method while the transport of neutrals relied on a mono-kinetic model. The differences in term of accuracy of the transport model of ions should not be overstated, however, because the large numerical diffusion in velocity space due to the finite difference method used to solve Vlassov equation in the hybrid model may have actually led to a worse estimation of the velocity dispersion than in the fluid model which presents a very limited numerical diffusion.

In spite of all differences between the models, the results are in surprisingly close agreement as can be seen from Fig.1. The explanation lies certainly in the relatively modest contribution of walls to the overall mobility of electrons in this range of discharge voltage because of the low secondary electron emission of the material taken into account. Note that while both models strongly differ on the treatment of wall conductivity, they do describe the bulk conductivity in a similar way.

### 3.4 Influence of the material of the channel

#### 3.4.1 Qualitative differences between materials

Three material have been considered in this study, referred as *Mat-A*, *Mat-B* and *Mat-C*.

As mentioned earlier, the effect of backscattering could only be accounted for in a qualitative way. On the basis of the discussion given in section 2.3, the backscattered energy yield was taken as a linear function of the effective SEE yield at zero energy:

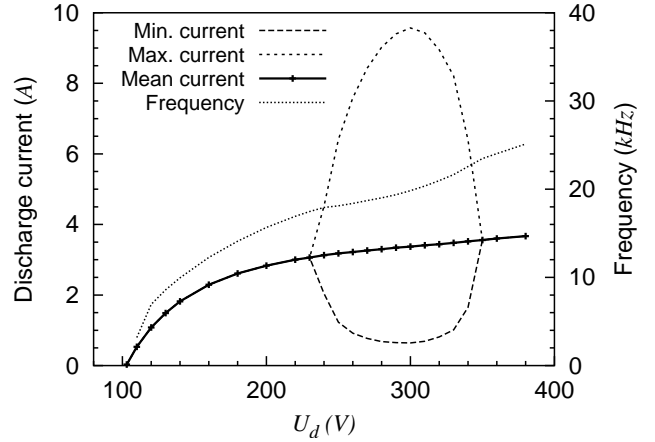
$$\tau_{bs} = \alpha \cdot \delta_{eff}(0) \quad \alpha \leq 1$$

The factor  $\alpha$  was arbitrarily set to  $\frac{2}{3}$ , assuming that elastic backscattering dominates at low energy. The estimation of backscattered energy rates gives the following inequality:

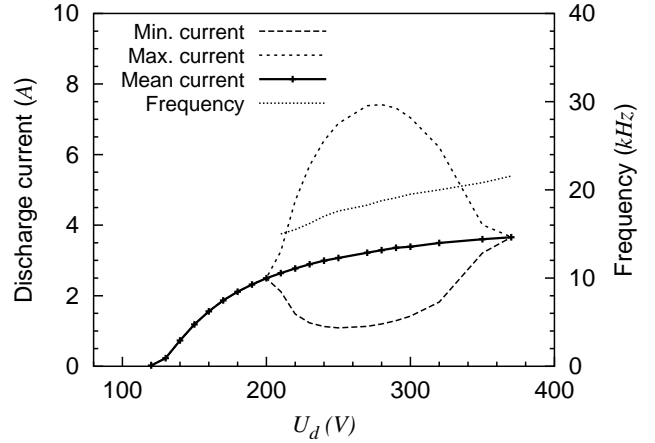
$$\tau_{bs}|_{Mat-A} < \tau_{bs}|_{Mat-B} < \tau_{bs}|_{Mat-C}$$

The backscattered energy rate of *Mat-A* is actually almost twice lower than with other materials.

Regarding electron secondary emission, *Mat-B* is characterized by a much lower cross-over energy and in



(a) present work (SPT-100ML)



(b) from J.P. Boeuf and L. Garrigues (SPT-100)

Figure 1: Comparison of the computed discharge current (mean value and envelope of oscillations) and frequency of oscillations obtained (a) in the present study taking  $W_B = 1.2 \cdot W_B^0$  and (b) in [23] for a standard SPT-100. The mass flow rate is in both cases  $Q = 5mg.s^{-1}$ .

general a higher SEE yield than the two other materials. The ordering in term of cross-over energies is:

$$\varepsilon^*|_{Mat-B} < \varepsilon^*|_{Mat-C} < \varepsilon^*|_{Mat-A}$$

### 3.4.2 Phenomenology

Without entering into details (which will be done in section 3.5), the three main regions that can be distinguished in the simulated CVC of each material can be described as follows:

1. The *bulk conductivity regime*: at low discharge voltage, the sheath voltage is high and electron-wall collisions consequently infrequent. Electron transport is therefore realized mainly through electron-neutral collisions.
2. The *electron temperature saturation regime*: at intermediate discharge voltage, the increase of electron temperature causes the sheath voltage to diminish, inducing large electron energy losses at the walls. The intensity of these losses increases very rapidly, preventing the temperature from overcrossing the critical temperature at which the sheath becomes space-charge limited. The temperature consequently saturates and the saturation is progressively extended to the whole acceleration zone as the voltage is increased
3. The *space charge limited sheath regime*: when the discharge voltage is high enough, the sheath potential finally saturates, and the temperature overcrosses the critical value. In this regime, the electron-wall collisions frequency become very large and induces an electron avalanche at the walls responsible for a high discharge current and high Joule losses strongly impacting the efficiency of the thruster.

The exact position of each region in the CVC strongly depends on the SEE properties of the channel. The separation between the two first regions cannot be localized very accurately, but the passage to the space charge limited sheath regime occurs within a very narrow voltage range and easily characterized by an inflection point (vanishing second derivative) in the CVC.

### 3.4.3 Discussion of the simulated CVC

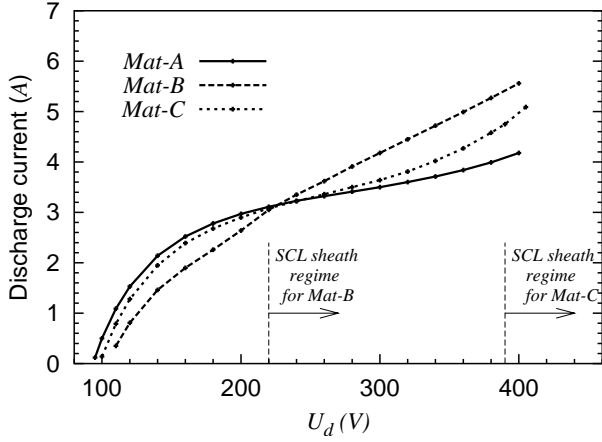
The computed CVC for channels made of different materials with and without backscattering effects are given in Fig.2. They can be compared to the experimental results reproduced in Fig.3.

It can be seen that with *Mat-B*, the space charge limited (SCL) sheath regime is reached as soon as  $U_d = 200V$ , while it is never reached with a *Mat-A* in the range of voltage considered. *Mat-C* exhibits clearly the characteristics of all three regimes mentioned above.

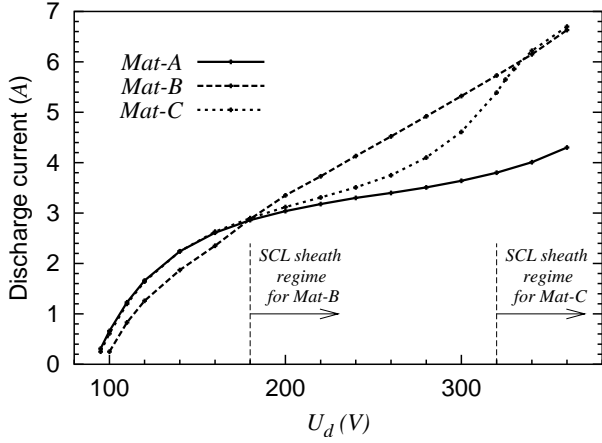
As expected, the agreement with experimental measurements is rather poor in the region below 200V. It is however interesting to note that even if the quantitative values are very underestimated, the relative order between the values of discharge current for different materials is consistent with experiments, which tends to show that even if walls do not play a direct role in the anomalous conductivity, they still provide a non-negligible contribution to the mobility at low voltages.

Above 200V approximately, the passage to a SCL regime with *Mat-B* causes a rapid increase of the total current, while with *Mat-C* the departure from the bulk conductivity regime becomes sensitive. With *Mat-A*, the beginning of the temperature saturated regime starts only at the end of the voltage range considered. If not perfect, the qualitative agreement with experimental results of Fig.3 in this region is nevertheless very reasonable, especially when backscattering is taken into account. In particular, the discharge current with *Mat-C* indeed reaches a value close to that of *Mat-B* at higher voltage, i.e. when the SCL sheath regime is entered. The saturation of discharge current observed with *Mat-A* is never strictly seen in simulations, but the value of the total current remains nevertheless very low, only slightly above the ion current. As it will be seen later, the temperature saturation regime does not seem to be observed in experiments with *Mat-A*, although the present results seem to confirm the existence of such a regime with *Mat-B*.

Even though backscattering is not strictly necessary to explain the qualitative differences between different materials, it does clearly lead to more realistic values. It should be kept in mind that  $U_d$  does represents only the voltage drop between anode and exit plane, which implies that even the results with backscattering are still too much shifted towards high voltages. A comparison of the CVC with and without backscattering reveals however a more fundamental effect, which is an enhanced differentiation between the behavior of *Mat-A* and *Mat-C* that may well explain the large differ-



(a) without backscattering



(b) with backscattering

Figure 2: Computed mean discharge current as a function of  $U_d$  for different ceramics (a) with  $\tau_{bs} = 0$  and (b) with  $\tau_{bs} = \frac{2}{3}\delta_{eff}(0)$  and at the nominal mass flow rate ( $Q = 5mg.s^{-1}$ ).

ences observed experimentally between the discharge currents obtained with these two materials. If the measured SEE can be relied upon, it seems indeed difficult to explain the very different behaviors between these materials only the basis of SEE yields. On the other hand, the extrapolated effective SEE yield at zero energy  $\delta_{eff}(0)$  and the mean atomic weight of each ma-

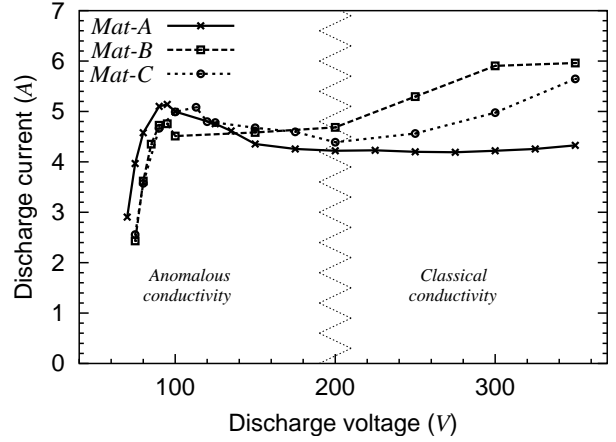


Figure 3: Experimental mean value of the discharge current as a function of the discharge voltage for different ceramics at a mass flow rate  $Q = 5mg.s^{-1}$  [1].

terial both tend to show that these two materials have very different backscattering yields, and these results give thus a tangible evidence that backscattering may play an important role in the behavior of the sheath and of the discharge as a whole.

#### 3.4.4 Comparison of frequencies

By contrast with experiments, no self-excited low-frequency oscillations were recovered with *Mat-B* and *Mat-C*, although a self-excited high frequency mode ( $300kHz - 1MHz$ ) with a phase velocity and a propagation direction related to the velocity of ions was very often obtained, in particular with *Mat-B*. A digital low-band filter was used when necessary in order to extract the low frequency and stationary characteristics of the discharge current. Such kind of oscillations were indeed reported in some experiments under the name of *transient-time* oscillations but it remains unclear whether the high-frequency mode seen in the model really has a physical meaning or originates from numerical instabilities.

Despite the disagreement on self-excited regions, a strong correlation was found between the eigenfrequency of the model and the fundamental frequency of the discharge measured experimentally. The results of simulation are given in Fig.4. Only the results of computations including backscattering have been reported,

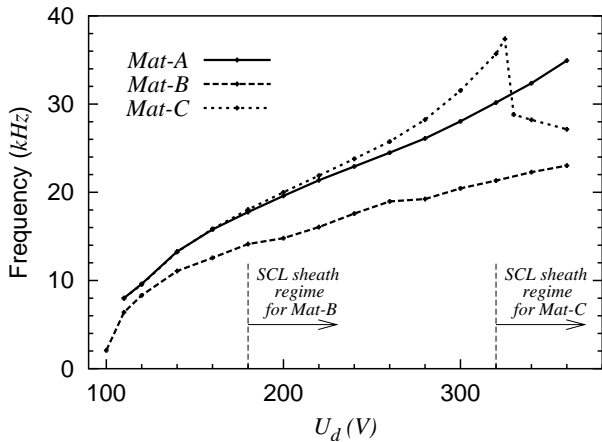


Figure 4: Computed eigenfrequency/oscillation frequency of the model as a function of  $U_d$  for different ceramics at the nominal mass flow rate ( $Q = 5\text{mg}\cdot\text{s}^{-1}$ ) taking into account backscattering.

since simulations without backscattering raise very similar results (except for a different scaling with respect to  $U_d$  similar to what is observed with the CVC).

A comparison with the frequency spectra of Fig.5 derived from experimental results exhibits many similarities between simulations and experiment. It is of course not always possible to make a clear parallel due to the fact that these spectra show in some place coexisting modes of distinct frequencies which are definitely not harmonics of the fundamental mode (this is in particular visible with *Mat-B*).

Both experiments and simulations show that the frequency variation with *Mat-A* is continuous and quasi linear in the whole range of discharge voltage. The correlation can be clearly seen from Fig.6 which compares the eigenfrequency of the model and the main frequencies obtained in [27] on the basis of the experimental records corresponding to Fig.5. The quantitative agreement may not be as good as it seems at first glance due to the fact that  $U_d$  is actually the discharge voltage between anode and exit plane while the experimental frequency is plotted along the total discharge voltage, but the quasi-linear growth of the frequency is properly recovered.

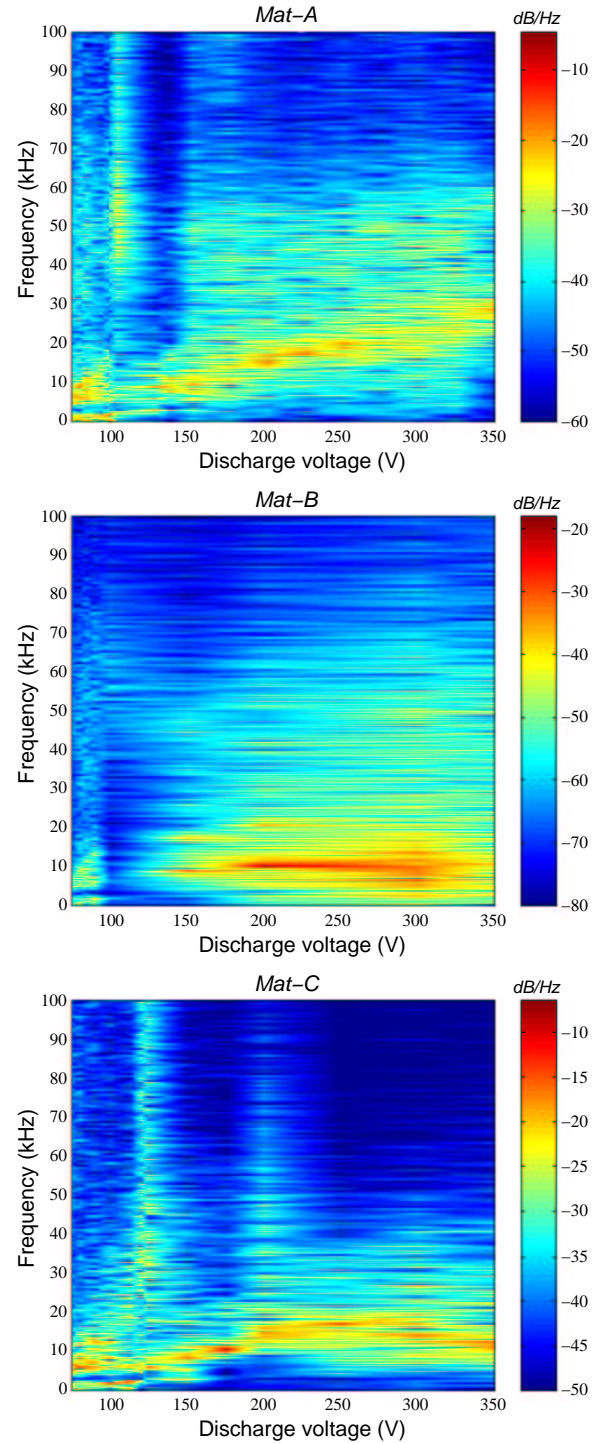


Figure 5: Frequency spectra of the oscillations of discharge current obtained by N. Gascon from experimental measurements with different ceramics [1].

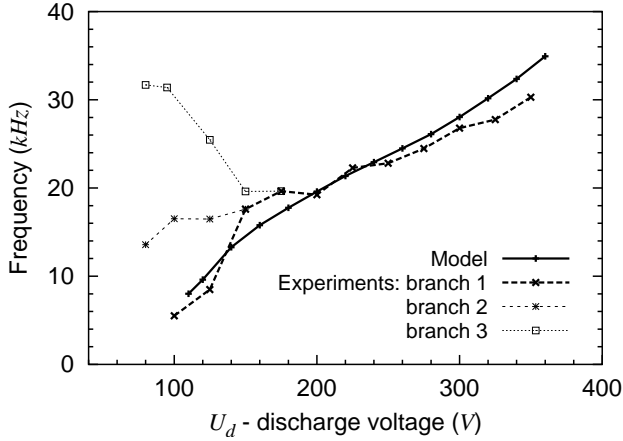


Figure 6: Comparison between the eigenfrequency of the model and the frequencies obtained in [27] from a Fourier analysis of experimental data [1] considering a channel made of *Mat-A* for  $Q = 5\text{mg}\cdot\text{s}^{-1}$ .

The frequency spectrum relative to *Mat-B* shows a fundamental frequency much lower than with other materials. Simulations seem to overestimate the frequency with this material, but the eigenfrequency obtained from the model is nevertheless sensitively lower than with *Mat-A* and *Mat-C*. Oppositely to what is seen with *Mat-C* and in the next section with *Mat-A*, the SCL sheath passage of *Mat-B* does not seem to lead to a decay of the frequency neither in experiments nor in the simulations. The reasons for this difference of behaviors between low SEE materials and high SEE materials is still being investigated.

*Mat-C* exhibits a more peculiar behavior: the sudden drop of frequency followed by a moderate steady decrease seen in the experimental frequency spectrum is well recovered by the model (although at a higher voltage) and is characteristic for the passage to a SCL sheath regime for materials with low SEE yields. It will be shown in the next section that this behavior can also be seen with *Mat-A* at higher voltage, and must probably be attributed to non-linearities rather than to a different oscillation mechanism.

### 3.5 Current-voltage characteristic of low SEE materials

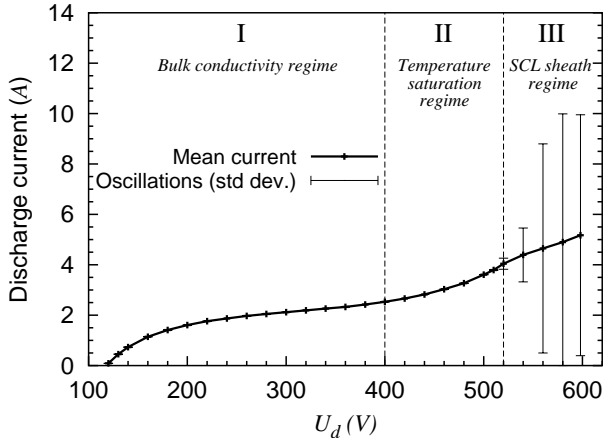
#### 3.5.1 Motivations and scope

Due to its low secondary emission, the SCL regime of *Mat-A* could not be observed in the voltage range investigated in the previous section. The high voltage region which has been studied experimentally in [1] at low mass flow rate with *Mat-A* is therefore of tremendous importance for the investigation of a possible space charge limited regime with low SEE materials. A comparison of numerical results at low mass flow rate (Figs.7 and 10) with experimental results (Figs.8 and 11) suggest that the space charge limited regime is indeed observed experimentally and is somehow even more strongly characterized than in simulations.

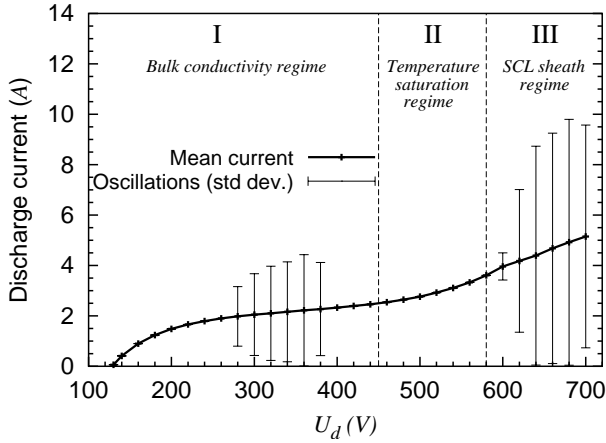
Let us precise that backscattering was neglected in this study since it is quite small for *Mat-A* and would not add much insight to the discussion. Its sole effect in the case of *Mat-A* is to shift the CVC towards lower voltages, which would make the results quantitatively more realistic but would not modify the qualitative picture.

#### 3.5.2 Bulk conductivity regime

As observed earlier, the voltage range below 200V is poorly described by the model because of the presumed anomalous conductivity. Above 200V, the model predicts a linear increase of total current which actually corresponds to a stabilization of the ion current due to the completeness of ionization and to a steady increase of the electron current with  $U_d$  due to Ohm's law. This differs somewhat from experimental results, where a saturation of the total current is observed like in many experimental results relative to SPT-type thrusters. It can be noted that the value of the total current predicted by simulations remains lower than the saturated current measured in experiments, (at least in the bulk conductivity region), and it is therefore not impossible that the differential current be induced by the anomalous conductivity. The stabilization of the total current seen in experiments constitutes nevertheless an intriguing phenomenon. The quasi-linear growth of frequency in region 3. (*Fluctuations* region) bulk conductivity region is on the other hand reasonably well described by the model as in the previous section, and also provides a realistic quantitative estimation of the frequency in that region.



(a) nominal magnetic field



(b) wide magnetic region

Figure 7: Computed discharge current (mean value and envelope of oscillations) as a function of  $U_d$  for *Mat-A* and a mass flow rate  $Q = 3.5 \text{ mg} \cdot \text{s}^{-1}$  with (a)  $W_B = W_B^0$  and (b)  $W_B = 1.2 \cdot W_B^0$ .

### 3.5.3 Temperature saturation regime

The largest discrepancies seem to occur in the temperature saturation region, which may correspond to region 4. in the experimental CVC, although its existence at all in the case of this material is questionable. The first discrepancy is the prediction by the model of a very strong damping (Fig.10) in this region, which is in striking

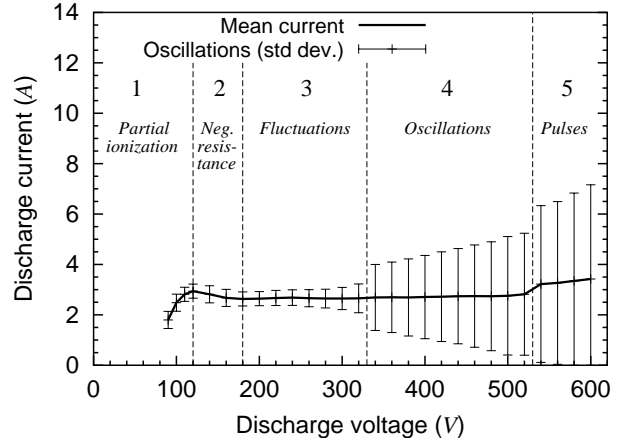


Figure 8: Experimental mean value and standard deviation of the discharge current as a function of the discharge voltage [1]. The thruster operates with *Mat-A* at a mass flow rate  $Q = 3.5 \text{ mg} \cdot \text{s}^{-1}$ .

contrast with the existence of self-excited oscillations in experiments. Just like in section 3.3, simulations do predict a likelihood for self-excited oscillations close to  $U_d = 300 \text{ V}$  as can be seen from the local minimum of the damping as well as from the CVC obtained with  $W_B = 1.2 \cdot W_B^0$  but the strong damping which invariably occurs close to the CSL sheath passage seems to prevent a junction between the two oscillating regions observed numerically. It is very possible that the one-dimensionality of the model spoils the transient behavior in this regime since the presheath obviously plays a fundamental role at such a high voltage due to dominating plasma/wall interactions, and the mode responsible for the oscillations in this regime is therefore probably not purely axial. The fact that the simulated discharge current rapidly increases in this region is also inconsistent with experimental observations. These discrepancies are difficult to explain since experimental results seemed to support the existence of a temperature saturation regime in the case of *Mat-C*.

The frequency stabilizes in experiments while it continues its linear growth in simulations, but this may not be due to a problem of the model. A probable explanation of this stabilization is that the large oscillations which appear in experiments emphasize strong non-linear effects due to the non-monotonic dependency

of the sheath potential on the temperature close to the SCL sheath passage. It can indeed be observed in simulations that oscillations *always* lead to a decrease of the frequency. A slight manifestation of this effect can be seen in the oscillatory region of Fig.1 (a) in spite of the fact that non-linearities are not very strong in the bulk conductivity regime, but the most striking effect of non-linearities will be apparent in the SCL sheath regime, now to be discussed.

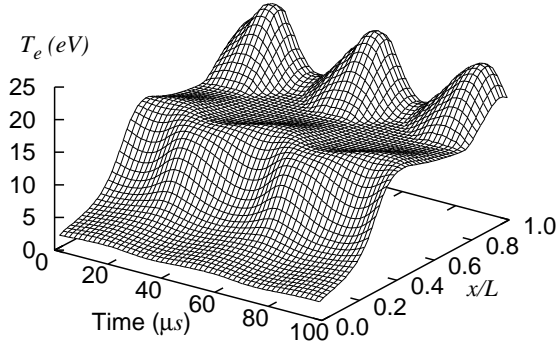


Figure 9: Typical transient behavior of the electron temperature in an oscillatory SCL sheath regime.

### 3.5.4 SCL sheath regime

The sudden burst of oscillations when passing from region 4. to region 5. (*pulses* region) appears very probably as the counterpart of the beginning of a strong oscillatory regime seen in region *III.* of the model, namely in the SCL sheath regime. The fast increase of the discharge current within the SCL sheath passage seen in simulations is surprisingly even more localized in experimental results.

A very interesting aspect of the SCL sheath regime is the fast decay of frequency seen both in experiments and in simulations, which provides a very complementary confirmation of the correlation between the pulses regime and the SCL sheath regime.

The current understanding of this peculiar behavior of the frequency reposes on the observation that non-linearities are extremely strong in SCL sheath regime. Indeed, it can be seen from Fig.9 that in the presence of oscillations there exists a region of the channel where

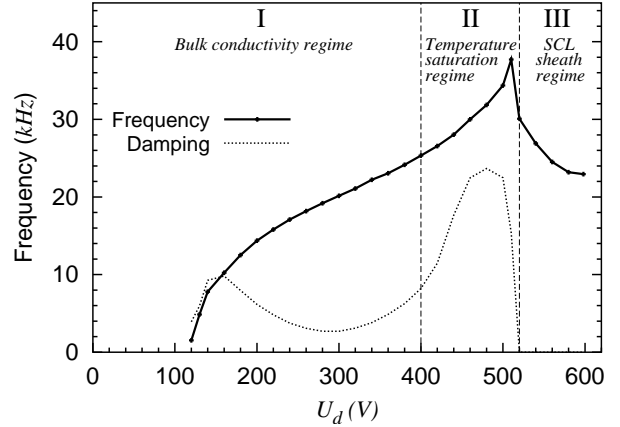


Figure 10: Computed eigenfrequency/oscillation frequency and damping of the model as a function of  $U_d$  for *Mat-A* at a mass flow rate  $Q = 3.5 \text{ mg.s}^{-1}$  with the nominal magnetic field.

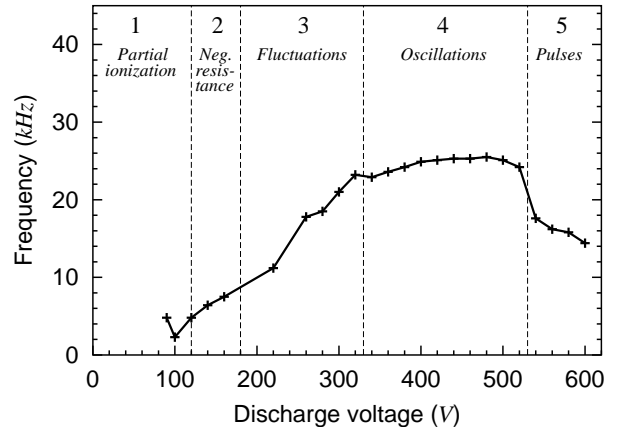


Figure 11: Experimental value of the main frequency of the oscillations of the discharge current as a function of the discharge voltage [1]. The thruster operates with *Mat-A* at a mass flow rate  $Q = 3.5 \text{ mg.s}^{-1}$ .

the temperature actually alternates between saturation (the plateau of Fig.9) and the SCL sheath regime (the “bumps” of Fig.9). Such a behavior is observed even for very small amplitude oscillations, which is why a decay of the eigenfrequency could be observed with *Mat-C* even though there were no self-excited oscillations.

It is nevertheless clear both from experiments and from simulations that the decrease of the frequency

within the SCL sheath regime is very much related to the amplitude of oscillations, which is in no way surprising since stronger oscillations necessarily induce larger non-linear effects.

A corollary of these observations is that the drop of frequency in the SCL sheath regime does not discard the validity of the predator-pray theory suggested in [28] to explain low frequency oscillations. The mechanism of oscillations in the SCL sheath regime is the same that controls low-frequency oscillations at lower voltage, but the simple predator-pray model based on linearized transport equations is not valid any longer to predict the frequency due to the highly non-linear behavior of the discharge

### 3.5.5 Synthesis

The region 5. of the experimental CVC was clearly identified as the SCL sheath regime due to the simultaneous correlation between a fast increase of the discharge current, the presence of a strong oscillatory regime and a sudden decrease of frequency.

The linear part of the bulk conductivity regime probably corresponds to the current saturation regime of experiments, that is region 3. and possibly region 4. It was suggested that the first self-oscillating region of simulations (observed for a wide magnetic region, but always underneath as can be seen from the damping) may correspond to region 4. of the experimental CVC. There remain however many doubts with respect to this last hypothesis, due to the fact that the two self-excited regions of the experimental CVC are connected, which never seems to be the case in simulations due to a strong damping associated with the temperature saturation regime.

This, and the general lack of correlation between the temperature saturation regime and region 4. of the experimental CVC may mean that the temperature saturated regime is not observed experimentally with *Mat-A* even though it seems to exist with *Mat-C* which presents a slightly lower SEE cross-over energy. It is difficult at this point to propose an explanation for these disparate behaviors.

## 4 Conclusion

Many aspects of the current-voltage characteristic of Hall thrusters were recovered in simulations using a 1D model of the discharge. In particular, it was shown that most of the effects observed experimentally with channels made of different materials can be interpreted on the basis of the secondary electron emission yield and of the electron backscattering yield of the channel. The presence of a space charge limited sheath regime suggested in [3] seems to be confirmed and was identified in simulation and experiments as a high discharge current / low frequency mode sometime associated with strong oscillations. The oscillations in this region are still ruled by a predator-pray mechanism, but the linearized predator-pray model which predicts a continuous growth of the frequency with increasing voltage is invalidated due to the strong non-linearities induced by a non-monotonic behavior of the sheath.

This work leaves several questions open concerning among others the near-perfect discharge current saturation observed experimentally with some materials and the correspondence between the oscillatory regions seen in simulation and experiments. Some of the discrepancies observed may be due to limitations inherent to 1D modeling, since the anomalous conductivity is likely to involve azimuthal waves while the role of the presheath at high discharge voltages suggests a strong dependence of the discharge on the radial direction. Other processes that were neglected in this study like multiple ionization events could also partly explain the poorer agreement between simulations and experiments at very high discharge voltages.

## Acknowledgements

This work was performed in the frame of the projects 8-T07A-028-21 and 8-T12D-015-21 funded by the Polish Committee for Scientific Research (KBN) and with the support of Groupement De Recherche CNRS/CNES/SNECMA/ONERA no 2232 « Propulsion à plasma pour systèmes spatiaux ». A fellowship for N. Gascon is provided by the European Space Agency.

## References

- [1] N. Gascon, "Etude de propulseurs plasmiques à effet Hall pour systèmes spatiaux. Performances, propriétés des décharges et modélisation hydrodynamique", PHD Thesis, Université de Provence (France), December 2000.
- [2] K. Makowski, S. Barral, Z. Peradzynski, M. Dudeck "Influence of the plasma/wall interactions on the operation of Hall thrusters", proceedings of the third International Conference on Spacecraft Propulsion, pp. 377-383, Cannes (France), October 2000.
- [3] L. Jolivet, J.-F. Roussel, "Effects of the secondary electron emission on the sheath phenomenon in a Hall thruster", proceedings of the third International Conference on Spacecraft Propulsion, pp. 367-, Cannes (France), October 2000.
- [4] J.A. Syage, "Electron impact cross sections for multiple ionization of Xenon and Krypton", Phys. Rev. A 26 no 9, 1992.
- [5] R.M. Myers, D.H. Manzella, "Stationary Plasma Thruster plume characteristics", 23rd International Electric Propulsion Conference, IEPC 93-053, Seattle, September 1993.
- [6] N. Sadeghi, N. Dorval, J. Bonnet, D. Pigache, C. Kadlec-Philippe, A. Bouchoule, "Velocity Measurements of  $Xe^+$  in Stationary Plasma Thruster using LIF", 35th AIAA/ASME/SAE/ASEE Joint Propulsion Conference & Exhibit, AIAA Paper 99-2429, Los Angeles, June 1999.
- [7] K. Makowski, Z. Peradzynski, S. Barral, M. Dudeck, "Effect of approximate energy balance in Stationary Plasma Thruster", 36th AIAA/ASME/SAE/ASEE Joint Propulsion Conference & Exhibit, AIAA Paper 2000-3658, Huntsville, Alabama, July 2000.
- [8] A.V. Phelps, compilation of collision cross-sections for different gases, available on-line: <ftp://jila.colorado.edu>
- [9] A. Jablonski, C. Jansson, S. Tougaard, "Elastic electron backscattering from surfaces: prediction of maximum intensity", Physical Review B, Vol. 47 nb 12, pp 7420-7430, March 1993.
- [10] P.G.T. Howell, K.M.W. Davy, A. Boyde, "Mean atomic number and backscattered electron coefficient calculations for some materials with low mean atomic number", Scanning Vol. 20, pp 35-40, 1998
- [11] E.J. Sternglass, "Backscattering of kilovolt electrons from solids", Physical Review Vol. 95 nb 2, pp 345-358, July 1954
- [12] K. Makowski, Z. Peradzynski, S. Barral, M. Dudeck, "Fluid model of plasma inside a Stationary Plasma Thruster", submitted to Plasma Source Science and Technology.
- [13] E. Ahedo, P. Martinez-Cerezo, M. Martinez-Sanchez, "Model of plasma-wall interaction effects in a Hall thruster", 37th AIAA/ASME/SAE/ASEE Joint Propulsion Conference & Exhibit, AIAA Paper 2001-3323, Salt Lake City, July 2001.
- [14] G.D. Hobbs, J.A. Wesson "Heat flow through a Langmir sheath in the presence of electron emission", Plasma Physics, Vol. 9, pp 85-87, 1967
- [15] A.I. Morozov, "Steady-state uniform Debaye sheaths", Sov. Journal of Plasma Physics, vol. 17, No 6, pp 393-397, 1991
- [16] D.C. Joy, "A database on electron-solid interactions", Scanning vol. 17, pp 270-275 1995
- [17] M. Dapor, A. Miotello, "Backscattering of electrons from selected oxides", Eur. Phys. J. AP 5, 143-148, 1999
- [18] V.Yu. Fedotov, A.A. Ivanov, G. Guerrini, A.N. Vesselovzozof, M. Bacal, "On the electron energy distribution function in a Hall thruster", Physics of Plasma, Vol. 6, No 11, pp. 4360-4365, 1999

- [19] E. Ahedo, P. Martinez, M. Martinez-Sanchez, "Steady and linearly-unsteady analysis of a Hall thruster with an internal sonic point", 36th AIAA/ASME/ SAE/ASEE Joint Propulsion Conference & Exhibit, AIAA Paper 2000-3655, Huntsville, July 2000.
- [20] S. Roche, N. Gascon, M. Prioul, L. Magne, S. Béchu, A. Bouchoule, P. Lasgorceix, D. Pagnon, C. Pérot, L. Albarède, M. Touzeau, M. Dudeck, M. Lyszyk, "Operating conditions and plasma study of an ATON-class Hall thruster", proceedings of the third International Conference on Spacecraft Propulsion, pp. 351-, Cannes (France), October 2000.
- [21] P.L. Roe, "Approximate Riemann solvers, parameter vectors, and difference schemes", *Journal of Computational Physics* 43(2), pp. 357-372, 1981.
- [22] A. Harten, "High resolution schemes for hyperbolic conservation laws", *Journal of Computational Physics* 49, pp. 357-392, 1983.
- [23] J.P. Boeuf, L. Garrigues, "Low frequency Oscillations in a Stationary Plasma Thruster", *J. Appl. Phys.*, Vol. 84, N°7, 1 October 1998.
- [24] S. Bechu, C. Perot, N. Gascon, P. Lasgorceix, A. Hauser, M. Dudeck, "Operating Mode Investigations of a Laboratory Stationary Plasma Thruster", 35th AIAA/ASME/ SAE/ASEE Joint Propulsion Conference & Exhibit, AIAA- 99-2567, Los Angeles, June 1999.
- [25] E. Choueiri, "An overview of plasma oscillations in Hall thrusters", proceedings of the third International Conference on Spacecraft Propulsion, pp. 287-303, Cannes (France), October 2000.
- [26] V.D. Olendarev, "Stationary plasma thrusters mathematical model", 26th International Electric Propulsion Conference, IEPC 99-110, Kitakyushu (Japan), October 1999.
- [27] J. Kurzena, N. Gascon, M. Dudeck, V. Lago, A. Lebéhot, "Oscillations of discharge current in a Stationary Plasma Thruster", 3rd French Polish Seminar on Plasma Physics, Warsaw, September 2001
- [28] J.M. Fife, M. Martinez-Sanchez, J. Szabo, "A numerical study of low-frequency oscillations in Hall thrusters", 33rd AIAA/ASME/ SAE/ASEE Joint Propulsion Conference & Exhibit, AIAA-97-3051, Seattle, 1997